Engineering Structures 327 (2025) 119680

Contents lists available at ScienceDirect

Engineering Structures

journal homepage: www.elsevier.com/locate/engstruct

Concurrent optimization of truss structures and build directions for multi-axis additive manufacturing

Jun Ye [a], Xiaoyang Lin [b], Hongjia Lu [c,d,*], Linwei He [e], Guan Quan [b], Cheng Huang [f], Paul Shepherd [g]

[a] School of Civil Engineering, University of Leeds, Leeds LS2 9JT, UK
[b] College of Civil Engineering and Architecture, Zhejiang University, Hangzhou 310058, China
[c] Future City (Intelligent Industrial Construction) Laboratory, Innovation Center of Yangtze River Delta, Zhejiang University, Jiaxing 314100, China
[d] Centre for Innovative Structures and Materials, School of Engineering, RMIT University, Melbourne 3001, Australia
[e] Department of Civil and Structural Engineering, University of Sheffield, Sheffield S1 3JD, UK
[f] Department of Civil and Environmental Engineering, Imperial College London, London SW7 2AZ, UK
[g] Department of Architecture & Civil Engineering, University of Bath, Bath BA2 7AY, UK

ARTICLE INFO

Keywords:
Multi-axis additive manufacturing
Structure optimization
Self-support structures
Printing path planning

ABSTRACT

Additive manufacturing (AM) has undergone rapid development over the past decade, yet printing parts with overhangs still poses a critical challenge, restricting the fabrication of components with arbitrary geometries. In structural optimization, incorporating overhang constraints can mitigate this issue. However, prior research has predominantly focused on 3-axis machines, leaving multi-axis capabilities insufficiently explored. These conventional 3-axis approaches often necessitate considerable trade-offs in structural material consumption. To overcome this, our study introduces a novel two-step optimization method tailored for multi-axis AM, which uses an optimized structure from traditional layout optimization as the starting point. The first step involves decomposing the design domain into multiple zones and solving a novel optimization problem to identify optimal local build directions for each zone, aiming to maximize the structure's printability. If the printability is still not satisfactory, we proceed to a second step, which refines the structure and build directions to minimize overhanging elements. Our examples validate the effectiveness of the proposed method, showing that the substantial performance sacrifices typically associated with 3-axis approaches are reduced to less than 7 % with our multi-axis AM-based approach.

1. Introduction

Additive manufacturing (AM) technology has undergone significant advancements over the years and is now employed in a variety of industries including construction, mechanical engineering, aerospace, and biomechanics [1–5]. A wide range of materials can be used, including plastics, metals [6], and ceramics [7]. However, most 3D printing currently relies on a 3-axis configuration, which has a fixed build direction perpendicular to the printing platform, necessitating support structures for overhanging parts. The support structures result in extra material consumption and removing the support structures can potentially damage the printed component [8]. To overcome these issues, multi-axis configurations have been developed in recent years. These configurations incorporate a rotatable base platform that enables the variation of build directions during the printing process. As a result, the local build directions can be customized to mitigate the overhang effect. Therefore, studies related to multi-axis AM have become an active area of interest in recent years.

The majority of multi-axis AM studies focus on tool-path planning. For example, Li et al. [9] proposed a vector field-based approach for curved layer slicing, with the goals of eliminating support structures, preventing collisions, and improving the mechanical properties of the printed component. Dai et al. [10] suggested a two-stage decomposition approach for overcoming overhang issues in multi-axis AM. This method first separates the target component into curved print layers and then further decomposes them into curved print paths. Xu and Li [11,12]

* Corresponding author at: Future City (Intelligent Industrial Construction) Laboratory, Innovation Center of Yangtze River Delta, Zhejiang University, Jiaxing 314100, China.
E-mail address: hongjia.lu@rmit.edu.au (H. Lu).

https://doi.org/10.1016/j.engstruct.2025.119680
Received 12 April 2024; Received in revised form 18 August 2024; Accepted 6 January 2025
Available online 13 January 2025

have also proposed decomposition methods that involve dividing a given structure into multiple individual parts, and then employing different build directions for each part to avoid overhanging structural parts. While studies have made significant contributions to reducing the support structures and printing time with multi-axis AM [13], they consider path planning for given structures or components. To further unleash the potential of multi-axis AM, it can be incorporated into the structural optimization to yield self-supportable structures associated with superior structural performance.

Structural optimization plays a pivotal role in automated design. Initiated by Michell's optimality criteria [14], this field has seen the development of numerous methods over the years. These methods fall into two primary categories: discrete truss optimization and continuum topology optimization. Continuum structural optimization, introduced by Bendsøe et al. [15], has branched into various methodologies including the Solid Isotropic Material with Penalization-based approach (SIMP) [16], the Bi-directional Evolutionary Structural Optimization (BESO) [17,18], level-set approach [19–21], Moving Morphable Components (MMC) [22–25], and Moving Morphable Voids (MMVs) [26,27]. In contrast, discrete truss optimization uses a point-line discretization, known as the ground structure approach [28], which traditionally incurs high computational costs and tends to produce complex structures, particularly in 3D contexts. To mitigate this, Gilbert and Tyas [29] introduced a 'member-adding' method to reduce computational costs while maintaining optimal solutions. He et al. [30] further enhanced this with a geometry optimization method, rationalizing structural layouts. Currently, layout optimization efficiently yields effective conceptual designs [31,32]. When comparing the continuum approach with the discrete approach, the continuum approach allows for the design of structures with a wide range of geometric features. To achieve truss-like structures, it typically uses high mesh resolution, a low volume fraction, and a small density filter radius [33]. In contrast, the discrete approach, which relies on point-line discretization, can efficiently produce truss structures at a lower computational cost. Given that the overhang effect is more pronounced in truss structure problems with low volume fractions [34], this study focuses on the truss discrete optimization approach.

Previously, various structural optimization approaches have been investigated to reduce the overhang effect in 3-axis AM. One of the most prevalent approaches in continuum topology optimization is the density-based method, which evaluates the printability of individual elements based on the presence of nearby elements. Based on this method, Gaynor et al. [35] proposed a wedge-shaped filter approach for designing self-supporting structures adopting regular meshing (i.e., square elements), and Garaigordobil et al. [36] used an edge-detection method to identify and eliminate overhang features in optimized structures. Langelaar [37,38] integrated the support relationship between adjacent elements into topology optimization to eliminate unsupported elements, while Van de Ven et al. [39,40] employed front-propagation techniques. In the field of discrete truss optimization, He et al. [41] incorporated angle constraints into the traditional layout and geometry truss optimization approach to achieve overhang-free truss structures. While these methods effectively generate self-supporting structures, they primarily rely on 3-axis AM, which can lead to considerable performance compromises when addressing overhang constraints. Therefore, multi-axis AM can be employed to reduce performance compromises.

On the combination of truss structure optimization and multi-axis AM, Lu et al. [42] proposed to first decompose the design domain into a number of zones and then use an optimization approach to determine the local build direction for each zone; later it is extended to 2D topology optimization [43]. However, Lu et al. [42] focused on 2D truss structures and the optimized results were not physically validated. Therefore, in this study, we propose improvements to make the approach applicable to 3D problems, and then physically validate the results with a multi-axis AM machine. The remainder of the article is arranged as follows: Section 2 introduces the overhang problem and the collision problem to be considered in multi-axis AM; Section 3 first reviews the previous 2D approach, and then introduces the newly proposed 3D method; Section 4 presents numerical examples to demonstrate the effectiveness of the proposed method; Section 5 presents a physical validation of an optimized structure; Section 6 provides relevant discussions and conclusions.

2. Additive manufacturing with multi-axis configuration

The research presented in this paper focuses on multi-axis AM. For the sake of completeness, we first introduce several related concepts and parameters in this section.

2.1. Definition of maximum overhang angle

In AM, components are built through a layer-by-layer deposition process. During this process, materials situated in overhanging positions are susceptible to collapse due to gravity. Specifically, when the angle between the build direction and the incline direction of the member exceeds the maximum overhang angle $\phi_{\max}$ (Fig. 1), the deposited material fails to consolidate, which reduces the printing quality or prevents the formation of the component. The value of $\phi_{\max}$ depends on the adopted configuration (i.e., printing material and deposition approach etc.). Generally, $\phi_{\max} = 45^{\circ}$ is used for plastic materials, and $20^{\circ} \leq \phi_{\max} \leq 30^{\circ}$ is reported for the metal directed energy deposition (DED) process [44].

2.2. Base platform rotation of multi-axis AM

As shown in Fig. 2(a), a multi-axis AM machine consists of a printing nozzle attached to a robot arm and a rotatable base platform. The rotatable base platform allows different build directions during the printing process, enabling the use of customizable curved printing surfaces. Nevertheless, even when horizontal printing surfaces are adopted, multi-axis AM increases the value of $\phi_{\max}$ for local deposition positions (Fig. 2(b) & (c)), providing an improved ability to cope with the overhang effect. It is important to emphasize that since the overhang effect is caused by gravity, altering the relative angle between the printing component and gravity is only achievable through the rotation of the base platform. The robotic arm, in contrast, does not mitigate the overhang effect.

2.3. Collision problem in multi-axis AM

In 3-axis AM, the build direction is fixed, leading to flat and parallel printing surfaces as illustrated in Fig. 3(a). This configuration effectively eliminates the risk of collision between the printing nozzle and the already printed structure during the process [45]. In contrast, multi-axis AM allows the build direction to change throughout the printing, producing curved printing surfaces. While these curved surfaces can be

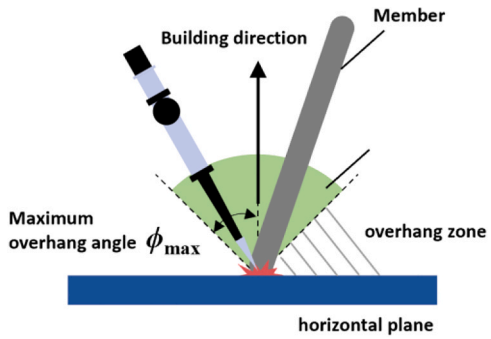

Fig. 1. maximum overhang angle $\phi_{\max}$.

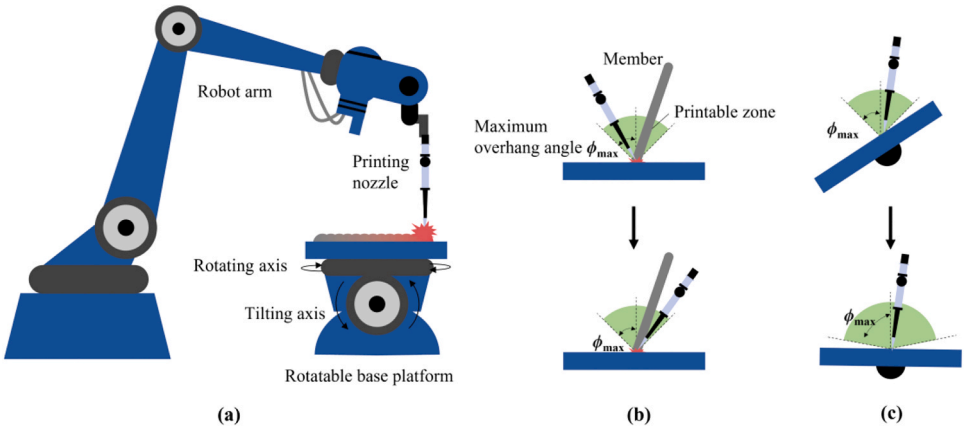

Fig. 2. The effect of structure overhang angle on print quality: (a) multi-axis AM machine (b) $\phi_{\max}$ is not changed when the arm is rotated in 3-axis printing. (c) platform rotation allows $\phi_{\max}$ to be increased in multi-axis printing, where $\phi_{\max}$ denotes maximum overhang angle.

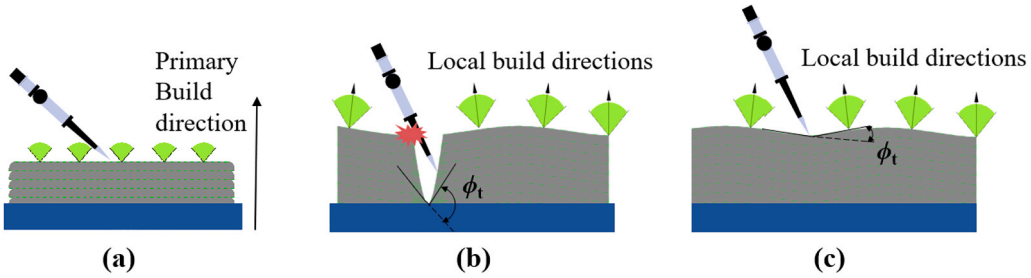

Fig. 3. Collision problem for 3- and multi-axis printing: (a) flat printing surfaces have no collision risk (b) slight concave printing surfaces have low collision risk (c) deep concave surfaces have high collision risk, where ϕ_t denotes turning angle.

tailored to minimize the overhang effect, they also introduce a risk of collisions, especially when the printing surface's concavity is significant (with a large turning angle ϕ_t as shown in Fig. 3(b)). Therefore, ϕ_t can be restricted to reduce the collision risk (Fig. 3(c)).

3. Numerical method

This study addresses the overhang constraints in the context of multi-axis AM, with the goal of achieving self-supportable structures that exhibit superior performance. We begin with a lower bound solution obtained from traditional layout optimization (i.e., without the overhang constraint) and then incorporate the overhang constraint via the following two-step approach:

(i) Print surface identification for a given structure

In this step, we start with a given optimized structure and then apply a novel linear optimization approach to determine the curved printing surfaces that maximize the structural printable ratio (i.e., overhang-free volume divided by total volume). Notably, since the structure itself remains constant during this step, full printability cannot be guaranteed. If the printable ratio is not satisfactory, we proceed to Step (ii).

(ii) Concurrent optimization of both structure and print surfaces

Step (ii) makes further improvements through a non-linear geometry optimization process that concurrently adjusts both the structure and the printing surfaces. With the added design freedom for structural form variation, both the printable ratio and the structural volume can be further improved. Notably, it is crucial to complete Step (i) before Step (ii), as the non-linear problem requires a feasible starting point to improve solution optimality. For this reason, we use the optimized solution from Step (i) as the initial input for Step (ii).

Since the structural optimization is based on the traditional layout and geometry optimization approach, these approaches are first reviewed in Section 3.1. Secondly, the 2D multi-axis approach [42] is briefly reviewed in Section 3.2. Finally, the newly developed 3D approach is introduced in Sections 3.3 to 3.5.

3.1. The layout and geometry optimization approaches on truss structures

The discrete layout optimization method provides a robust approach for creating highly efficient structures tailored to specific boundary conditions. This method typically involves three stages, as depicted in Fig. 4(a-c): initially defining the boundary conditions (Fig. 4(a)), then generating nodes and members to establish a 'ground structure' (Fig. 4(b)), and finally, determining the optimal layout (Fig. 4(c)) through solving a designated optimization problem:

$$\min_{\boldsymbol{a},\,\boldsymbol{q}} V = \mathbf{l}^{\mathrm{T}}\boldsymbol{a} \tag{1a}$$

$$\text{s.t. } \mathbf{B}\boldsymbol{q}_{\alpha} = \mathbf{f}_{\alpha} \tag{1b}$$

$$-\sigma^{-}\boldsymbol{a} \le \boldsymbol{q}_{\alpha} \le \sigma^{+}\boldsymbol{a} \tag{1c}$$

$$\boldsymbol{a} \ge \mathbf{0}, \tag{1d}$$

where $\mathbf{l} = [l_1, l_2, \cdots, l_m]^{\mathrm{T}}$ is the vector of member lengths; $\boldsymbol{a} = [a_1, a_2, \cdots, a_m]^{\mathrm{T}}$ represents the vector of member cross-sectional areas, with m indicating the total number of members; the internal force vector for the αth load case is denoted by $\boldsymbol{q}_{\alpha} = [q_{1,\alpha}, q_{2,\alpha}, \cdots, q_{m,\alpha}]^{\mathrm{T}}$, where forces are defined as positive for tension and negative for compression; V is the total volume of the structure; $\mathbf{B}$ represents the equilibrium matrix. $\mathbf{f}_{\alpha}$ is the nodal load vector for the load case α; σ^{-} and σ^{+} denote the ultimate strength of the material in compression and tension, respectively.

Eq. (1) represents a linear programming problem, effectively solvable using interior point methods [46]. However, structures optimized through the truss layout method often exhibit complexity. To address

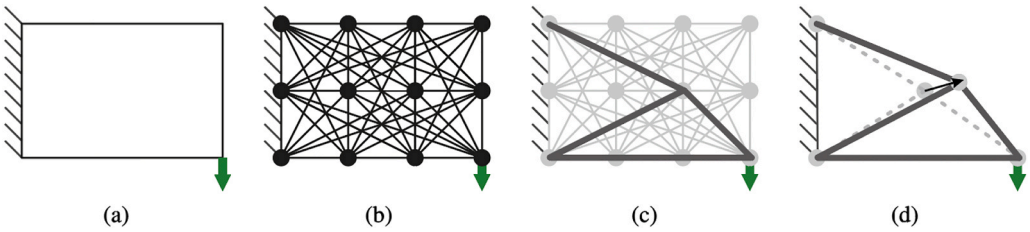

Fig. 4. The truss layout and geometry optimization process: (a) establishing the boundary conditions; (b) generating the ground structure; (c) identifying the optimized structural layout and (d) rationalizing the structure through node adjustment.

this, geometry optimization [30] can be applied for further structural rationalization (Fig. 4(d)). This method also incorporates nodal coordinates as variables. The optimization formulation is detailed below:

$$\min_{\boldsymbol{a},\,\boldsymbol{q},\,\boldsymbol{x},\,\boldsymbol{y}} V = \boldsymbol{l}(\boldsymbol{x},\boldsymbol{y})^{\mathrm{T}}\boldsymbol{a} \tag{2a}$$

$$\text{s.t. } \mathbf{B}(\boldsymbol{x},\boldsymbol{y})\boldsymbol{q}_{\alpha} = \mathbf{f}_{\alpha} \tag{2b}$$

$$-\sigma^{-}\boldsymbol{a} \le \boldsymbol{q}_{\alpha} \le \sigma^{+}\boldsymbol{a} \tag{2c}$$

$$\boldsymbol{a} \ge \mathbf{0}, \tag{2d}$$

where $\boldsymbol{x} = [x_1, x_2, \ldots, x_d]^{\mathrm{T}}$ and $\boldsymbol{y} = [y_1, y_2, \ldots, y_d]^{\mathrm{T}}$ represent the x- and y-coordinates of nodes, respectively, with d indicating the total number of nodes.

The structure obtained from Eqs. (1) serves as the initial point in Eqs. (2). Geometric modifications, such as forming crossovers and merging nodes, are implemented to rationalize the structure. Additional information about the geometry optimization process is available in [30].

3.2. Review of the 2D printing surface identification approach

The method employed in this paper is based on the 2D approach outlined by Lu et al. [42]. For a comprehensive understanding, a brief review of this method is provided in this section. It starts with the division of the design domain into multiple rectangular zones, each presumed to have a unique build direction. The build direction for each zone is then determined by evaluating the orientations of structural members within that specific zone.

The method for determining the local build direction for each zone is illustrated in Fig. 5. In Zone (2, 1), both members have their own printable ranges, represented by the green regions. When a common printable range exists, as shown in Fig. 5, any print direction within this range allows both members to be printed. If no common printable range is present, the build direction that maximizes the volume of printable members is preferred. Based on this concept, the following optimization problem can be solved to identify the local build directions that maximize the printable volume:

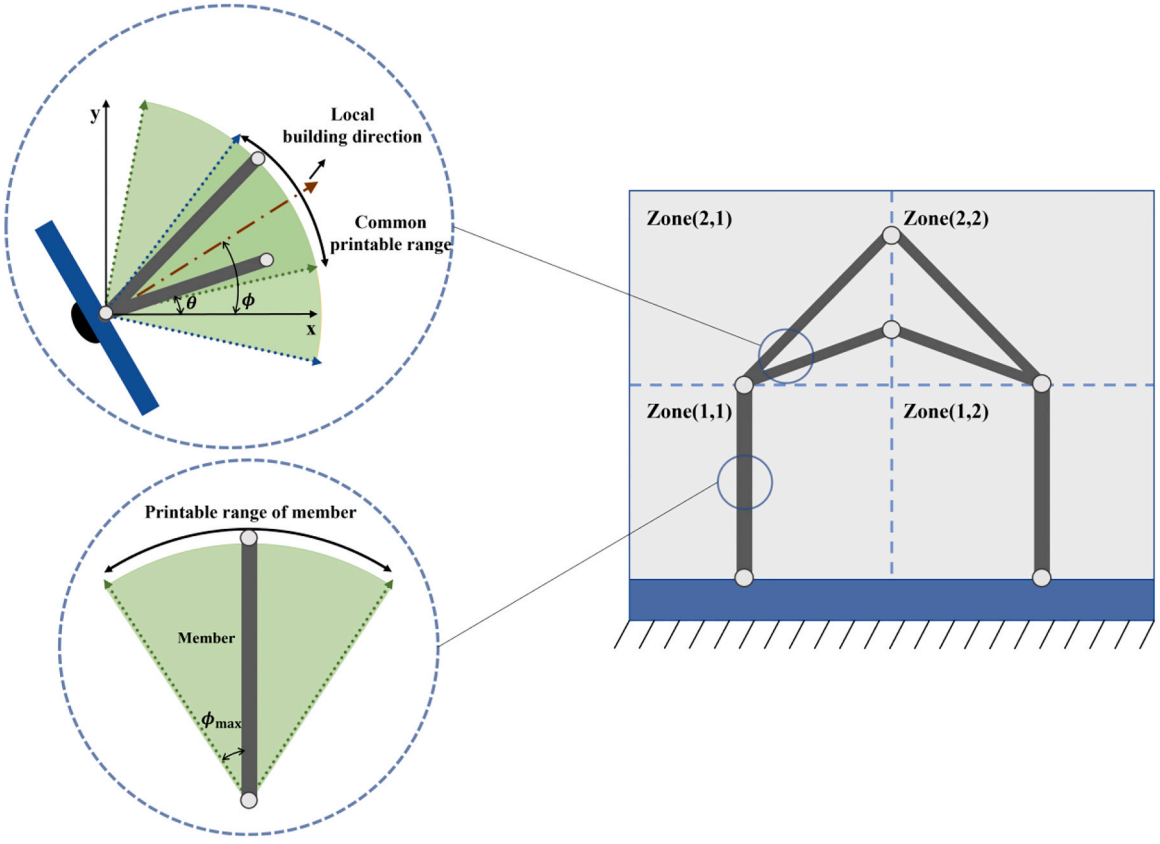

Fig. 5. Determination of member printing direction, where $\phi_{\max}$ is maximum overhang angle; ϕ is local build direction angle; θ denotes the orientation angle of each member.

$$\min_{\boldsymbol{\eta},\,\boldsymbol{\phi}} \eta_{\text{total}} = \sum_{\mu}\sum_{\nu} \boldsymbol{\eta}_{\mu,\nu}{}^{\mathrm{T}}\mathbf{v}_{\mu,\nu} \tag{3a}$$

$$\text{s.t. } \boldsymbol{\eta}_{\mu,\nu} = \left|\phi_{\mu,\nu}\mathbf{e} - \boldsymbol{\theta}_{\mu,\nu} - \phi_{\max}\mathbf{e}\right| + \left|\phi_{\mu,\nu}\mathbf{e} - \boldsymbol{\theta}_{\mu,\nu} + \phi_{\max}\mathbf{e}\right| - 2\phi_{\max}\mathbf{e}, \forall\mu \in \mathbb{Z}_{\mu}, \forall\nu \in \mathbb{Z}_{\nu} \tag{3b}$$

$$\boldsymbol{\phi}_{\mathrm{t}} \le \phi_{\mathrm{t,max}}\mathbf{e}, \tag{3c}$$

where η_{total} denotes the total overhang violation; $\boldsymbol{\eta}_{\mu,\nu}$ and $\mathbf{v}_{\mu,\nu}$ refer to the overhang angle violation vector and the member volume vector, with μ and ν denoting the zone row and column indices; n_{μ} and n_{ν} denote the numbers of rows and columns in the zones, respectively; $\mathbb{Z}_{\mu} = \{1, 2, \ldots, \mathrm{n}_{\mu}\}$ and $\mathbb{Z}_{\nu} = \{1, 2, \ldots, \mathrm{n}_{\nu}\}$ are row and column index sets; $\phi_{\mu,\nu}$ is the local build direction angle; $\phi_{\max}$ indicates the maximum allowable overhang angle; $\boldsymbol{\theta}_{\mu,\nu}$ is the member orientation angle; $\phi_{\mathrm{t,max}}$ represents the maximum printing surface turning angle and $\boldsymbol{\phi}_{\mathrm{t}} = [\phi_{1,2} - \phi_{1,1}, \cdots, \phi_{\mu,\nu} - \phi_{\mu,\nu-1}, \cdots, \phi_{\mathrm{n}_{\mu},\mathrm{n}_{\nu}} - \phi_{\mathrm{n}_{\mu},\mathrm{n}_{\nu}-1}]^{\mathrm{T}}$ denotes the turning angle vector; $\mathbf{e} = [1, 1, \ldots]^{\mathrm{T}}$ consists entirely of ones and of suitable length. Note that Eqs. (3) represent a linear programming problem, thus the identified solution is guaranteed to be globally optimal. More details of this formulation can be found in [42].

3.3. 3D printing surface identification approach

The 3D optimization approach adopts the same two-step scheme as the 2D approach. Firstly, it identifies the optimal printing surface for the designated structure. Subsequently, it concurrently optimizes both the structure and the printing surfaces. The first step requires the domain decomposition and other associated geometric constraints tailored for 3D problems, details of which are elaborated upon in Sections 3.3.1 to 3.3.5. The second concurrent optimization step is introduced in Section 3.4, and a summary is provided in Section 3.5.

3.3.1. 3D domain decomposition

Similar to the 2D approach, in the 3D problem, the design domain is first divided into a number of zones utilizing flat split planes as illustrated in Fig. 6.

3.3.2. Representation of 3D local build directions

In the 2D problem, the overhang violation $\boldsymbol{\eta}$ is computed utilizing the local build direction and the member orientation (Eq. 3(b)). For simplicity, in 3D problems, the local build direction and the member orientation are first projected onto two mutually perpendicular *xoz* and *yoz* planes (Fig. 7). Subsequently, the overhang violations for both the projection surfaces can be computed:

$$\beta = \left|\phi_x - \theta_x - \phi_{\max}\right| + \left|\phi_x - \theta_x + \phi_{\max}\right| - 2\phi_{\max} \tag{4a}$$

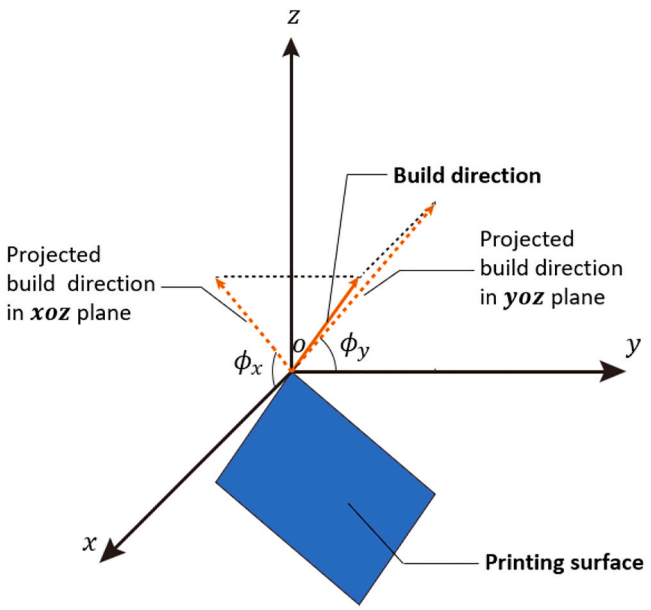

Fig. 7. Projection of the local print directions, where ϕ_x, ϕ_y represent the orientation angles of the projected local build directions, respectively.

$$\gamma = \left|\phi_y - \theta_y - \phi_{\max}\right| + \left|\phi_y - \theta_y + \phi_{\max}\right| - 2\phi_{\max}, \tag{4b}$$

where β and γ represent the projected overhang angle violation on the *xoz* and *yoz* planes, respectively; ϕ_x and ϕ_y denote the projection of local build direction onto the *xoz* and *yoz* planes, respectively; Similarly, θ_x and θ_y represent the projections of member orientations onto the *xoz* and *yoz* planes, respectively; $\phi_{\max}$ is the set maximum overhang angle.

It is worth noting that these two constraints lead to less conservative solutions, as when the projected intersection angles are equal to $\phi_{\max}$ in both the *xoz* and *yoz* planes, the real intersection angle is greater than $\phi_{\max}$. Nevertheless, the projection-based approach significantly reduces the numerical difficulty by making these two constraints linear. Moreover, we show in Section 5 that with the superior flexibility provided by multi-axis AM, the effect introduced by Constraints (4) is minor.

3.3.3. The collision problem for concave printing surfaces

As mentioned in Section 2.3, curved surfaces with large turning angles may cause potential collisions between the printing nozzle and already printed components. To address this problem, we use Constraints (5) to restrict the projected turning angles between neighbouring zones (i.e., Fig. 8):

$$\phi_{x,\mathrm{t}} \le \phi_{\mathrm{t,max}}\mathbf{e} \tag{5a}$$

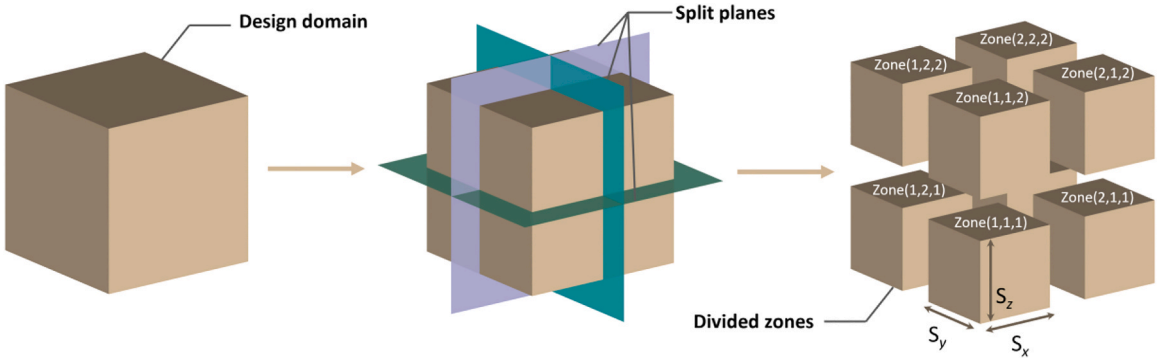

Fig. 6. Diagram of design domain zoning, where S_x, S_y, S_z represent the sizes of the divided zone, respectively.

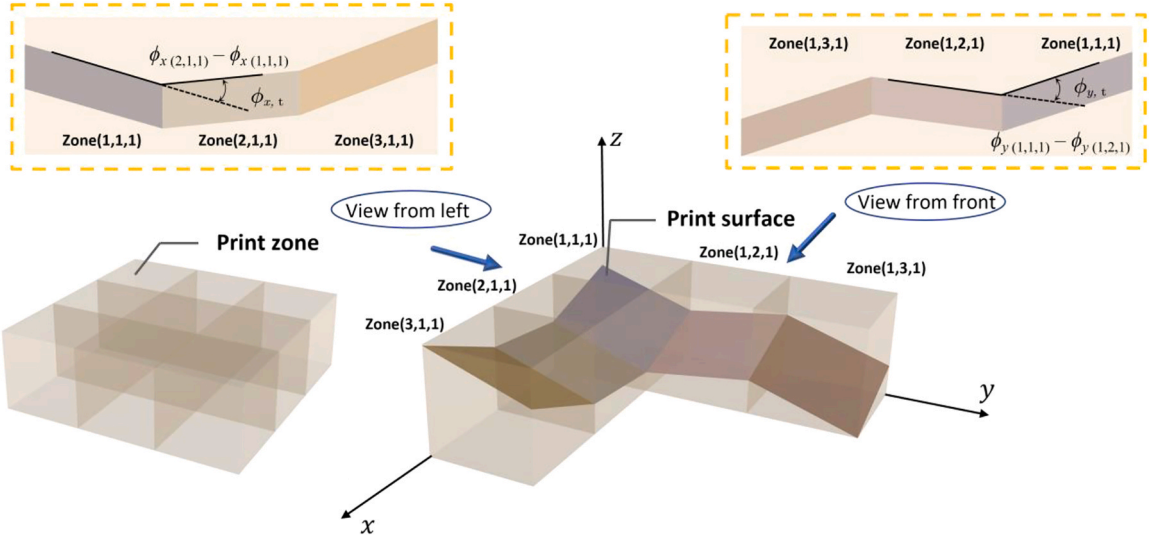

Fig. 8. Projection of the turning angle onto the *xoz* and *yoz* planes.

$$\phi_{y,t} \le \phi_{t,\max}\mathbf{e} \tag{5b}$$

3.3.4. Printing surface continuity constraint

Since the optimization considers only the local build directions, and the printing surfaces are generated by making them orthogonal to these directions after the optimization is complete, the resulting local printing surfaces may not form a continuous surface, regardless of the zone subdivision and sizes used. This potential discontinuity is illustrated in Fig. 9(a). The absence of this continuity means that the concavity of the printing surfaces cannot be controlled by Constraints (5), increasing the potential for collisions. To ensure the continuity of the surfaces, as demonstrated in Fig. 9(b), we apply Constraints (6) to the local build directions of adjacent zones, which ensures that neighbouring local surfaces share the same projection line on the intermediate surface:

$$\phi_{x,\,(i,\nu,w)} = \phi_{x,\,(j,\nu,w)},\ \forall (i,\,j) \in \mathbb{Z}_\mu, \forall \nu \in \mathbb{Z}_\nu, \forall w \in \mathbb{Z}_w \tag{6a}$$

$$\phi_{y,\,(\mu,k,w)} = \phi_{y,\,(\mu,l,w)},\ \forall (k,\,l) \in \mathbb{Z}_\mu, \forall \nu \in \mathbb{Z}_\nu, \forall w \in \mathbb{Z}_w, \tag{6b}$$

where $\phi_{x,(\mu,\nu,w)}$ and $\phi_{y,(\mu,\nu,w)}$ are the projected local build directions (i.e., Fig. 7), with μ, ν, w denoting the zone column, row and layer indices, respectively.

3.3.5. 3D printing surface optimization formulation

By applying the modifications introduced in Sections 3.3.1 – 3.3.4 to Problem (3), the 3D printing surface optimization problem can be expressed as follows:

$$\min_{\eta,\,\phi}\ \eta_{\text{total}} = \sum_{\mu}\sum_{\nu}\sum_{w} \boldsymbol{\eta}_{\mu,\nu,w}{}^{\mathrm{T}}\mathbf{v}_{\mu,\nu,w} \tag{7a}$$

$$\text{s.t. } \overline{\boldsymbol{\eta}}_{\mu,\nu,w} = \left|\boldsymbol{\phi}_{\mu,\nu,w} - \boldsymbol{\theta}_{\mu,\nu,w} - \phi_{\max}\mathbf{e}\right| + \left|\boldsymbol{\phi}_{\mu,\nu,w} - \boldsymbol{\theta}_{\mu,\nu,w} + \phi_{\max}\mathbf{e}\right| - 2\phi_{\max},\ \forall(\mu,\nu,w) \in \mathbb{Z} \tag{7b}$$

$$\phi_{x,\,(i,\nu,w)} = \phi_{x,\,(j,\nu,w)} \text{ and } \phi_{y,\,(\mu,k,w)} = \phi_{y,\,(\mu,l,w)},\ \forall (i,\,j) \in \mathbb{Z}_\mu, \forall (k,\,l) \in \mathbb{Z}_\nu, \forall (\mu,\,\nu,\,w) \in \mathbb{Z} \tag{7c}$$

$$\boldsymbol{\phi}_t \le \phi_{t,\max}\mathbf{e}, \tag{7d}$$

where $\boldsymbol{\eta}_{\mu,\nu,w} = \boldsymbol{\beta}_{\mu,\nu,w} + \boldsymbol{\gamma}_{\mu,\nu,w}$ and $\overline{\boldsymbol{\eta}}_{\mu,\nu,w} = \begin{bmatrix}\boldsymbol{\beta}_{\mu,\nu,w}\\ \boldsymbol{\gamma}_{\mu,\nu,w}\end{bmatrix}$ and with $\boldsymbol{\beta}_{\mu,\nu,w}$ and $\boldsymbol{\gamma}_{\mu,\nu,w}$ denoting the projected overhang angle violation vectors at *xoz* and *yoz* planes, respectively; $\boldsymbol{\phi}_{\mu,\nu,w} = \begin{bmatrix}\boldsymbol{\phi}_{x,(\mu,\nu,w)}\\ \boldsymbol{\phi}_{y,(\mu,\nu,w)}\end{bmatrix}$ with $\boldsymbol{\phi}_{x,(\mu,\nu,w)}$ and $\boldsymbol{\phi}_{y,(\mu,\nu,w)}$ representing the projected local build direction vectors; $\boldsymbol{\theta}_{\mu,\nu,w} = \begin{bmatrix}\boldsymbol{\theta}_{x,(\mu,\nu,w)}\\ \boldsymbol{\theta}_{y,(\mu,\nu,w)}\end{bmatrix}$ with $\boldsymbol{\theta}_{x,(\mu,\nu,w)}$ and $\boldsymbol{\theta}_{y,(\mu,\nu,w)}$ denoting the projected member orientation vectors; $\mathbb{Z} = \mathbb{Z}_\mu \times \mathbb{Z}_\nu \times \mathbb{Z}_w$ is the cartesian product of $\mathbb{Z}_\mu$, $\mathbb{Z}_\nu$

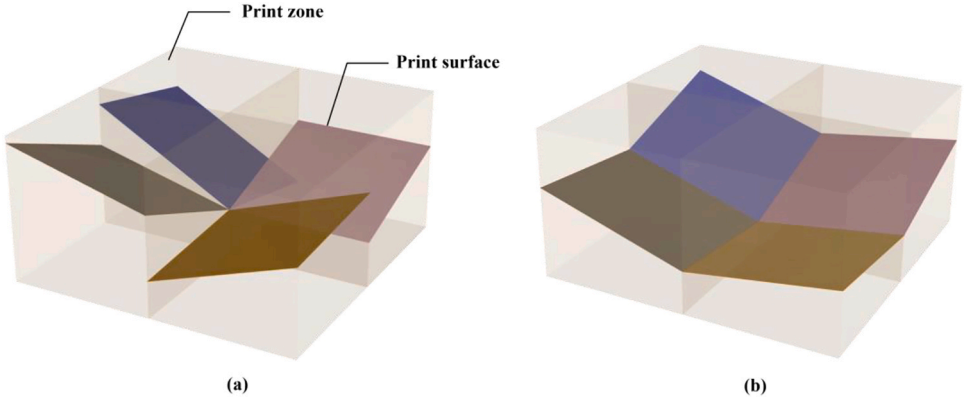

Fig. 9. Connectivity between the print surfaces in adjacent zones: (a) printing surface continuity is violated; (b) printing surface continuity is satisfied.

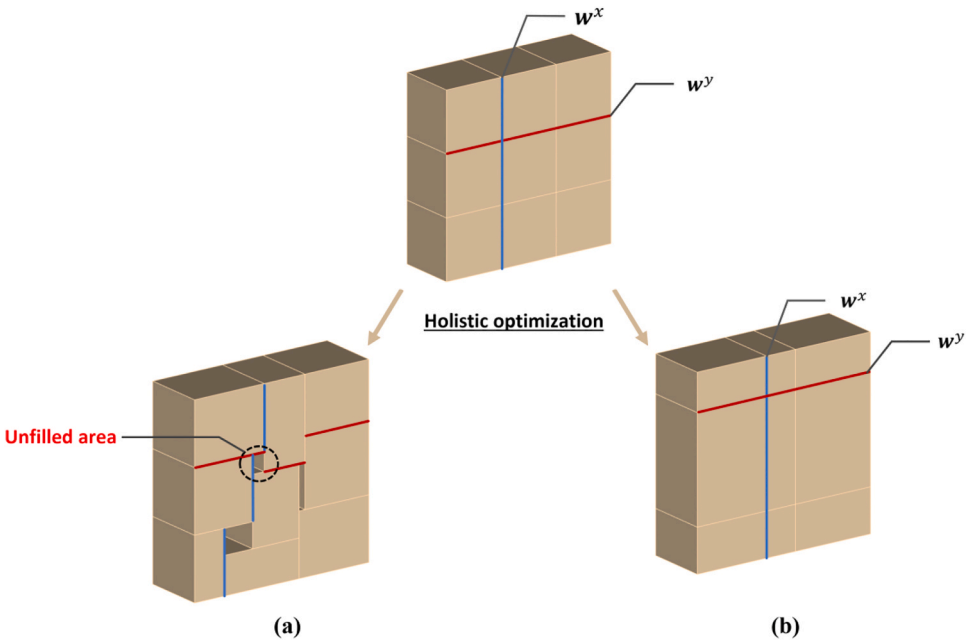

Fig. 10. The influence of boundary position variables of zones in the same layer on the optimization process: (a) considered as independent variables, which may lead to unfilled areas in the print layer; (b) shared boundary position vectors in the same row/column; here, $\boldsymbol{w}^x$ and $\boldsymbol{w}^y$ denote the boundary coordinates of the cubic zone in the x- and y-axis direction, respectively.

and $\mathbb{Z}_w$; $\phi_{\mathrm{t,max}}$ represents the maximum print turning angle and $\boldsymbol{\phi}_{x,\mathrm{t}} = [\phi_{x,(1,2,1)} - \phi_{x,(1,1,1)}, \cdots, \phi_{x,(n_\mu,n_\nu,n_w)} - \phi_{x,(n_\mu,n_\nu-1,n_w)}]^{\mathrm{T}}$ denote the x turning angle vector, and $\boldsymbol{\phi}_{y,\mathrm{t}}$ is derived using the same principle applied to the y-axis (i.e., Fig. 8).

By using two projected build directions in each zone, Eqs. (7) demonstrate a linear programming problem since the objective function and constraints are all linear, and the variables are continuous. This problem can be solved efficiently using a modern interior point solver [46]. This solver can be used as a black box, requiring the input of variable coefficients, variable bounds, and constraint bounds, and it guarantees a globally optimal solution. This approach ensures the identification of optimal printing surfaces in Step (i) (i.e., Eqs. (7)) and is also critical for Step (ii). The solution from Eqs. (7) provides the starting point for the non-linear programming in Step (ii), facilitating the enhancement of printing surface quality and, ultimately, leading to more efficient and printable final structures.

3.4. Concurrent optimization of the structure and build directions

While Eqs. (7) ensures a globally optimal solution, the identified printing surfaces may not guarantee a fully printable structure, as the target structure is predetermined. To address this problem, we propose an additional step to adjust the structure and the printing surfaces simultaneously, aiming to reduce or eliminate overhanging members. The optimization problem combines the geometry optimization that considers the nodal movement (i.e., Eqs. (2)) and the printing surfaces optimization problem (i.e., Eqs. (7)). In addition, the following two adjustments are introduced:

- Adjustment 1: The objective of obtaining an efficient structure with minimal overhang violation is achieved by penalizing the structural overhang violation with a factor p:

$$\min \boldsymbol{l}^{\mathrm{T}}\mathbf{a} + p\Big(\sum_{\mu}\sum_{\nu}\sum_{w}\boldsymbol{\eta}_{\mu,\nu,w}{}^{\mathrm{T}}\mathbf{v}_{\mu,\nu,w}\Big) \tag{8}$$

  Notably, instead of using the penalization approach, additional constraints to restrict the total overhang violation $\eta_{\mathrm{total}} = 0$ can also prevent overhang. However, because the starting point for the concurrent optimization is not fully printable, applying these overhang constraints would render the starting point infeasible. Since the non-linear programming problem requires a feasible starting point to reach solutions with high optimality, the penalization scheme shown in Objective function (8) is employed.
- Adjustment 2: We restrict the movement of each node to remain within its initially assigned zone in Constraints (9) and treat the zone boundaries as additional variables (i.e., $\boldsymbol{w}$). This approach ensures that the overhang violation for each member is calculated based on its original zone, while preserving design flexibility by allowing the zone boundaries to be adjustable.

$$\boldsymbol{w}^x_{\mu,\nu,w} \geq \boldsymbol{x} \geq \boldsymbol{w}^x_{\mu-1,\nu,w} \tag{9a}$$

$$\boldsymbol{w}^y_{\mu,\nu,w} \geq \boldsymbol{y} \geq \boldsymbol{w}^y_{\mu,\nu-1,w} \tag{9b}$$

$$\boldsymbol{w}^z_{\mu,\nu,w} \geq \boldsymbol{z} \geq \boldsymbol{w}^z_{\mu,\nu,w-1} \tag{9c}$$

In addition, during the optimization process, the void regions shown in Fig. 10(a) are not allowed. Thus, zones arranged in the same row/column are constrained to share the same boundary position variables $\boldsymbol{w}^x$ and $\boldsymbol{w}^y$ (i.e., Fig. 10(b)), and zones arranged in the same layer share the same $\boldsymbol{w}^z$. Furthermore, to prevent the zones from shrinking to infinitely small, the following constraints are used:

$$\boldsymbol{w}^x_{\mu-1,\nu,w} \geq \mathrm{w}_{x,\min}\mathbf{e} \tag{10a}$$

$$\boldsymbol{w}^{y}_{\mu,\nu,w} - \boldsymbol{w}^{y}_{\mu,\nu-1,w} \geq \mathrm{w}_{\mathrm{y,min}}\mathbf{e} \tag{10b}$$

$$\boldsymbol{w}^{z}_{\mu,\nu,w} - \boldsymbol{w}^{z}_{\mu,\nu,w-1} \geq \mathrm{w}_{\mathrm{z,min}}\mathbf{e} \tag{10c}$$

By combining Eqs. (2), Eqs. (7), Objective function (8), Constraints (9) and Constraints (10), the concurrent optimization formulation can be expressed as follows:

$$\min_{\boldsymbol{a},\boldsymbol{q},\boldsymbol{x},\boldsymbol{y},\boldsymbol{z},\boldsymbol{\eta},\boldsymbol{\phi}} \quad V + \overline{\eta}_{\mathrm{total}} = \mathbf{l}^{\mathrm{T}}\mathbf{a} + p\Big(\sum_{\mu}\sum_{\nu}\sum_{w}\boldsymbol{\eta}_{\mu,\nu,w}{}^{\mathrm{T}}\mathbf{v}_{\mu,\nu,w}\Big) \tag{11a}$$

$$\text{s.t.} \quad \mathbf{B}(\boldsymbol{x},\boldsymbol{y},\boldsymbol{z})\boldsymbol{q}_{\alpha} = \mathbf{f}_{\alpha} \tag{11b}$$

$$-\sigma^{-}\mathbf{a} \leq \boldsymbol{q}_{\alpha} \leq \sigma^{+}\mathbf{a} \tag{11c}$$

$$\mathbf{a} \geq \mathbf{0} \tag{11d}$$

$$\overline{\boldsymbol{\eta}}_{\mu,\nu,w} = \left|\boldsymbol{\phi}_{\mu,\nu,w} - \boldsymbol{\theta}_{\mu,\nu,w} - \phi_{\max}\mathbf{e}\right| + \left|\boldsymbol{\phi}_{\mu,\nu,w} - \boldsymbol{\theta}_{\mu,\nu,w} + \phi_{\max}\mathbf{e}\right| - 2\phi_{\max},\ \forall(\mu,\nu,w) \in \mathbb{Z} \tag{11e}$$

$$\phi_{x,\,(i,\nu,w)} = \phi_{x,\,(j,\nu,w)} \text{ and } \phi_{y,\,(\mu,k,w)} = \phi_{y,\,(\mu,l,w)},\ \forall(i,\,j) \in \mathbb{Z}_{\mu},\ \forall(k,\,l) \in \mathbb{Z}_{\nu},\forall(\mu,\nu,w) \in \mathbb{Z} \tag{11f}$$

$$\boldsymbol{\phi}_{t} \leq \phi_{\mathrm{t,max}}\mathbf{e} \tag{11g}$$

$$\boldsymbol{w}_{\mathrm{upp}} - \boldsymbol{w}_{\mathrm{low}} \geq \mathbf{w}_{\mathrm{min}} \tag{11h}$$

$$\boldsymbol{w}_{\mathrm{upp}} \geq \boldsymbol{X} \geq \boldsymbol{w}_{\mathrm{low}}, \tag{11i}$$

where $\overline{\eta}_{\mathrm{total}}$ denotes the penalized total overhang violation; $\boldsymbol{w}_{\mathrm{low}} = [\boldsymbol{w}^{x}_{\mu-1,\nu,w}, \boldsymbol{w}^{y}_{\mu,\nu-1,w}, \boldsymbol{w}^{z}_{\mu,\nu,w-1}]$ and $\boldsymbol{w}_{\mathrm{upp}} = \left[\boldsymbol{w}^{x}_{\mu,\nu,w}, \boldsymbol{w}^{y}_{\mu,\nu,w}, \boldsymbol{w}^{z}_{\mu,\nu,w}\right]$ are the boundary coordinate matrix; $\mathbf{w}_{\mathrm{min}} = [\mathrm{w}_{x,\mathrm{min}}\mathbf{e}, \mathrm{w}_{\mathrm{y,min}}\mathbf{e}, \mathrm{w}_{\mathrm{z,min}}\mathbf{e}]$ are lower bounds of the length of the cubic partition in the x, y and z directions. Constraints (11b), (11c), and (11d) originate from the layout optimization problem; Constraints (11e), (11f), and (11g) pertain to the printing surface optimization problem; while Constraints (11h) and (11i) are related to the geometry optimization. Due to the introduction of the nodal coordinate variables, Equations (11) become a non-linear programming problem. Hence the non-linear programming solver IPOPT is utilized to tackle this problem [47]. Notably, IPOPT requires gradient data to function. We compute the Jacobian and Hessian matrices using the symbolic computation package in Python, 'SymPy', to derive the analytical functions for the objective function and constraints. These derivative functions are then evaluated with the variable values and assembled into the Jacobian and Hessian matrices.

3.4.1. Obtain a starting point with reduced overhang

Since Eqs. (11) are non-linear and non-convex, the starting point significantly affects the quality of the final optimized result [48]. In this section, we propose an iterative approach to identify a starting point with reduced overhang for Eqs. (11), thereby improving the structural performance of the final optimized solution. This approach begins with the identified curved printing surfaces obtained from solving Eqs. (7). With the printing surfaces known, the projected overhang violations β and γ for every potential member in the ground structure can be calculated by evaluating Eqs. (4). In this step, if a member crosses multiple zones, the overhang angle violation is taken as the maximum value among those zones. Subsequently, we re-solve the layout optimization problem (2), penalizing each potential member by its corresponding overhang value:

$$\min_{\boldsymbol{a},\boldsymbol{q}} V = \sum_{\mu}\sum_{\nu}\sum_{w}\left(\mathbf{e} + p_0\boldsymbol{\eta}_{\mu,\nu,w}\right)^{\mathrm{T}}\mathbf{l}_{u,\nu,w}\mathbf{a}_{\mu,\nu,w} \tag{12a}$$

$$\text{s.t. } \mathbf{B}\mathbf{q}_{\alpha} = \mathbf{f}_{\alpha} \tag{12b}$$

$$-\sigma^{-}\mathbf{a} \leq \mathbf{q}_{\alpha} \leq \sigma^{+}\mathbf{a} \tag{12c}$$

$$\mathbf{a} \geq \mathbf{0}, \tag{12d}$$

where p_0 is the overhang violation penalty factor and $\mathbf{l}_{u,\nu,w}$ is a diagonal matrix of the lengths of the members.

Eqs. (12) result in efficient structures with reduced overhang, which can then be used as the target structure for Eqs. (7) to obtain a further improved printing surface. This iterative process continues until the maximum number of iterations is reached. Nevertheless, it is found that too many iterations and large p_0 lead to structures with low structural efficiency (see detailed investigation later in Section 4.1). For the current study, a maximum of 5 iterations has been found to yield satisfactory results. It is also worth noting that, firstly, Eqs. (12) are linear and can be solved using a modern interior point solver [46]; its efficiency can be further enhanced by the member-adding approach [29]. Secondly, although in some cases this iterative process eliminates overhang members, its design freedom is not as high as that of Eqs. (11), because the node and zone boundary positions are not variable in this approach. Therefore, the improved solution is used as the starting point for Eqs. (11) to further enhance structural efficiency and reduce overhang.

3.5. Workflow of the optimization method

The proposed optimization scheme includes the steps introduced in Sections 3.1, 3.3 and 3.4. For clarity, they are illustrated in Fig. 11.

4. Numerical examples

In this section, several examples are presented to demonstrate the effectiveness of the proposed approach. The proposed method η_{total} to represent the printability of a structure (i.e., Eq. 7(a)). In the following examples, a structure is considered printable when the total violation value is below a threshold of 0.1.

4.1. The influence of the penalty factor p_0

The penalty factor p_0 in Eq. (12a) determines the extent of the penalty imposed on overhanging members when the structure is reoptimized. To analyze the influence of the penalty factor, we solve the design problem in Fig. 12(a) with different values of p_0 ranging from 0.01 to 100. The maximum overhang angle is set to 50°, with a vertical zone size of $S_z = 2.0$ and horizontal zone sizes of S_x and $S_y = 1.0$, as shown in Fig. 12(b). A nominal lower bound solution obtained with the traditional layout optimization approach is shown in Fig. 12(c) and used to evaluate the volume sacrifice caused by the overhang constraints.

Fig. 12(e) displays the optimization results obtained with the approach in Section 3.2. The results indicate that the optimized structure contains unprintable members when p_0 values are set to 0.01 and 0.1. On the other hand, when p_0 is set to 10 or a larger number, although overhanging members are eliminated, the structural volume increases significantly. Therefore, a penalty factor within the range of 1.0–7.0 produces acceptable results in this example. The results demonstrate that a penalty factor that is too small may not adequately penalize constraint violations, resulting in not fully printable structures. Conversely, a penalty factor that is too large causes a considerable increase in material use, which makes the multi-axis AM-based approach behave similarly to the 3-axis-based approach in He et al. [41]. Additionally, to further demonstrate the impact of the iterative approach, as shown in Section 3.3, we present a solution obtained without the iterative approach in Fig. 12(d), which exhibits a 20.20 % increase in volume (i.e., relative to Fig. 12(c)). The noticeably larger volume of Fig. 12 (d) compared to the solutions in Fig. 12(e) (i.e., structures with p_0 between 1.0 and 7.0) demonstrates the benefits brought by the reconstruction process.

In the optimization process, curved printing surfaces can be generated for all the solutions shown in Fig. 12 (d - e). For clarity, we display the printing surfaces for the structure with $p_0 = 5.0$ in Fig. 13(a). Notably, in creating the physical structural model, we follow the approach outlined in [50], where nodal joints are represented as spheres with an expanded radius to accommodate overlapping structural volumes, and truss members are represented as cylinders with trumpet-shaped ends to ensure a smooth transition between members and joints. In the current study, the spherical joint is first merged with the member having the largest radius among all connected members, and then sliced using the printing surfaces of the merged member, as illustrated in Fig. 13(b). Following this strategy, the printing tool path for all the joints and members (Fig. 13(c)) can be obtained using the corresponding printing surfaces in Fig. 13(a).

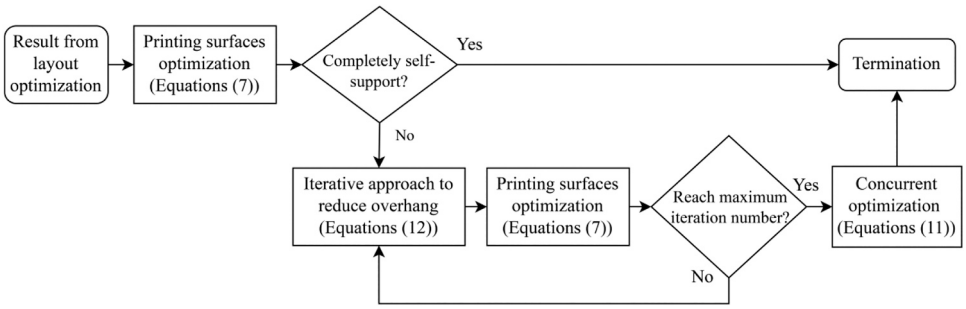

Fig. 11. Flow chart of the proposed algorithm.

4.2. The influence of maximum overhang angle

The maximum printable angle is a critical factor in AM. To demonstrate its influence on the optimized results, we use another cantilever example with the design domain and conditions shown in Fig. 14(a). The penalty factor p_0 is set to 4.0, S_x is set to 2.0, and S_y and S_z are set to 1.0. The maximum overhang angles are set to 45°, 50°, 55°, and 60°. The nominal design from the traditional layout and geometry optimization is

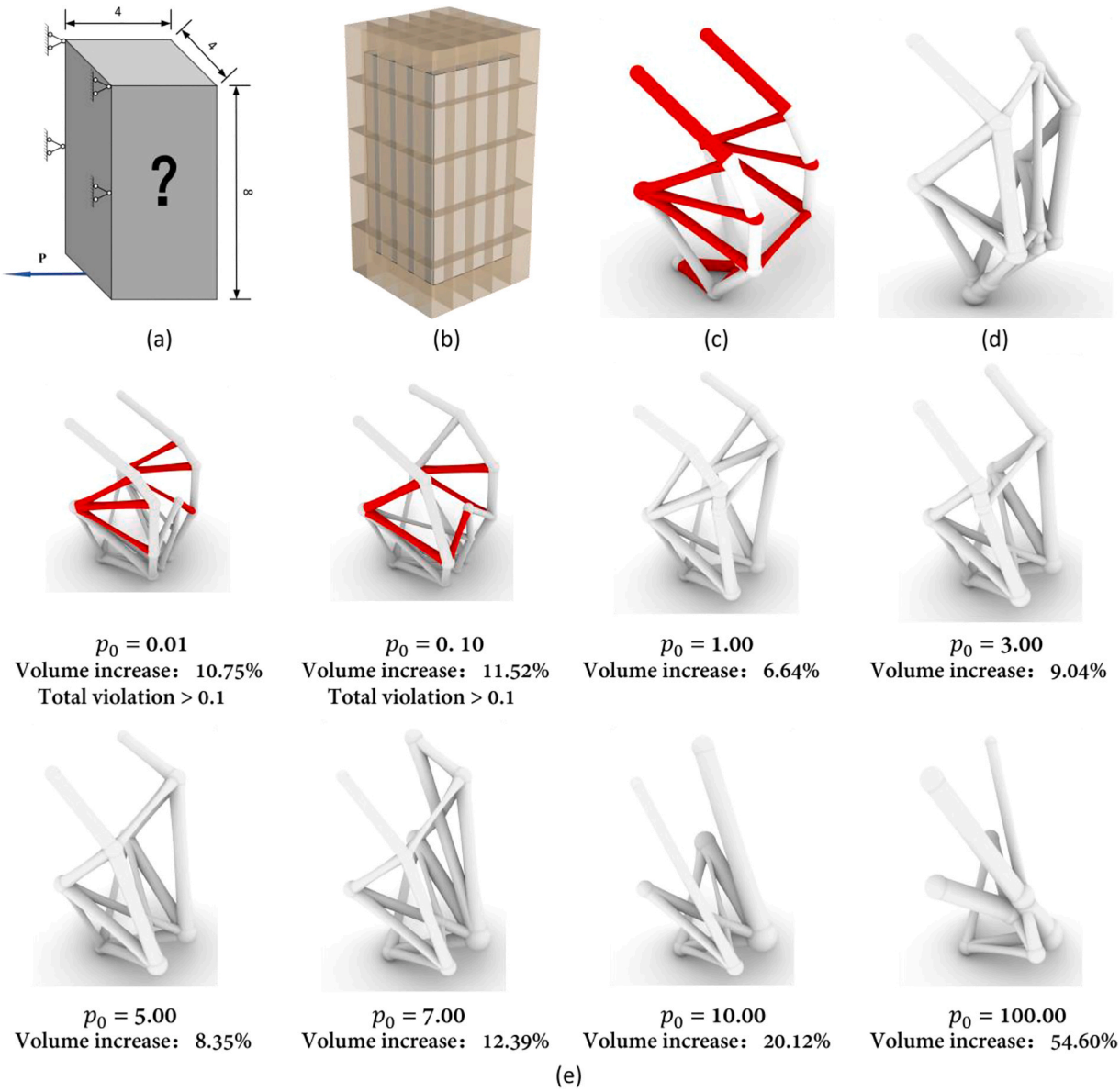

Fig. 12. Rotated cantilever example: (a) case description; (b) design domain decomposition; (c) nominal optimized structure, red members mean their overhang angle is higher than 50°; (d) 3D model of an optimized solution obtained without the reconstruction process, and the volume increase is 20.20 %; (e) optimization results of the example with different penalty factors, red members mean they cannot be printed.

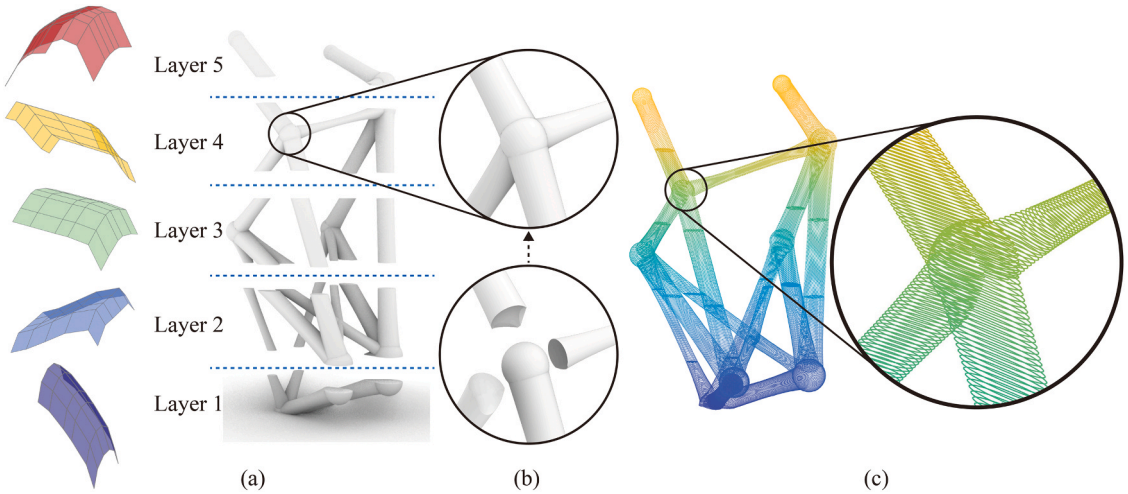

Fig. 13. Rotating cantilever example for $p_0 = 5.0$: (a) print surfaces for the five layers of the structure; (b) structural joint formed by spherical and trumpet-shaped elements; the sphere is unionid with the truss member with largest radius as shown in the decomposed view; (c) printing tool path obtained by slicing the structure with the curved printing surfaces shown in (a).

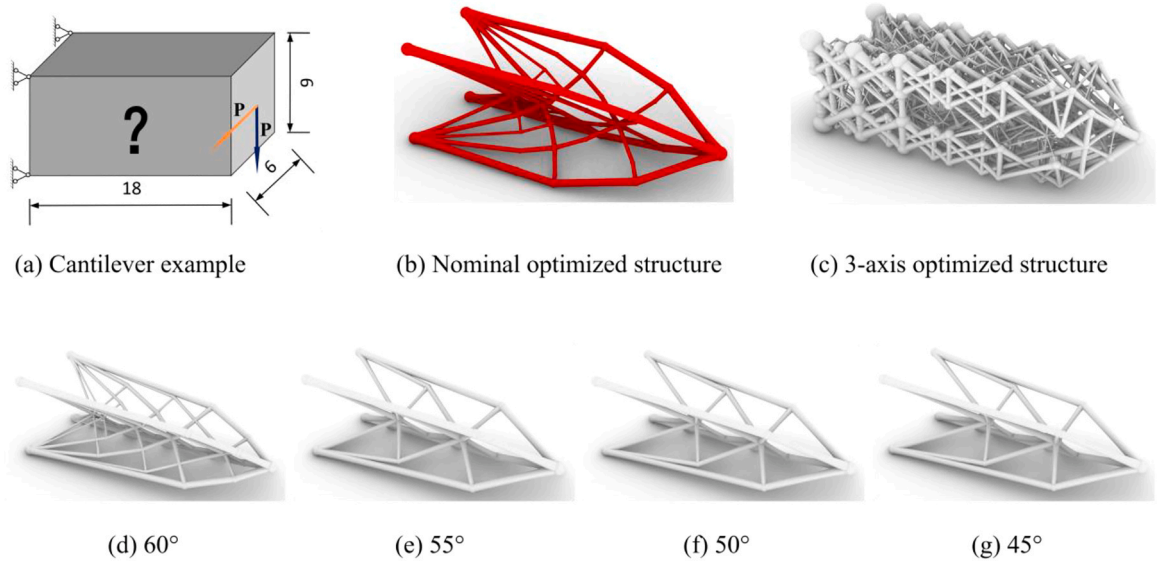

Fig. 14. Cantilever example: (a) case description (b) nominal optimized structure, red members mean their overhang angle is higher than 45°; (c) optimized structure with horizontal printing plan and 60° maximum overhang angle, the volume increase is 117.19 % compared to (b); (d) optimized structure with curved printing plan and 60° maximum overhang angle, the volume increase is 1.85 % compared to (b); (e) optimized structure with curved printing plan and 55° maximum overhang angle, the volume increase is 2.97 % compared to (b); (f) optimized structure with curved printing plan and 50° maximum overhang angle, the volume increase is 3.24 % compared to (b); (g) optimized structure with curved printing plan and 45° maximum overhang angle, the volume increase is 3.98 % compared to (b).

shown in Fig. 14(b). The optimized result obtained from the 3-axis optimization method is shown in Fig. 14(c), with the volume increased by 117.19 % compared to (b). With overhang constraint considered based on multi-axis AM, the optimized results are shown in Fig. 14(d - g), which are all self-supporting solutions. It can be seen that as the maximum overhang angle decreases, the structural volume increases and the bars in the structure tend to be more vertically oriented. Nevertheless, due to the enhanced flexibility provided by multi-axis AM, the volume increases (i.e., related to Fig. 14 (b)) in Fig. 14(d - g) are all less than 4 %.

4.3. The influence of zone size

The influence of domain decomposition on the optimized results is investigated in this section with the example shown in Fig. 15(a). For comparison, a nominal design without the overhang constraint considered is shown in Fig. 15(b) and a self-supporting structure designed with respect to 3-axis AM is shown in Fig. 15(g). Note that in the following examples, a maximum overhang angle of 45° is used.

We divide the investigation into two groups, in the first group, horizontal zone sizes S_x and S_y are fixed to 1.0 and vertical zone sizes S_z are varied from 1.0 to 4.0. The corresponding results are shown in Fig. 15(c - f). Among these results, $S_z = 3.0$ yields the structure with the lowest volume increase of 0.35 % and the most simplified layout. In the concurrent optimization step, since the structural nodes are restrained within their corresponding zone, an increase in the number of zone layers restricts the design freedom of concurrent optimization, resulting in high structural complexity and volume (Fig. 15(c)).

In the second group, S_z is fixed to 3.0 and S_x, S_y are changed from 0.5 to 4.0 (Fig. 16). The optimization results for different horizontal zone

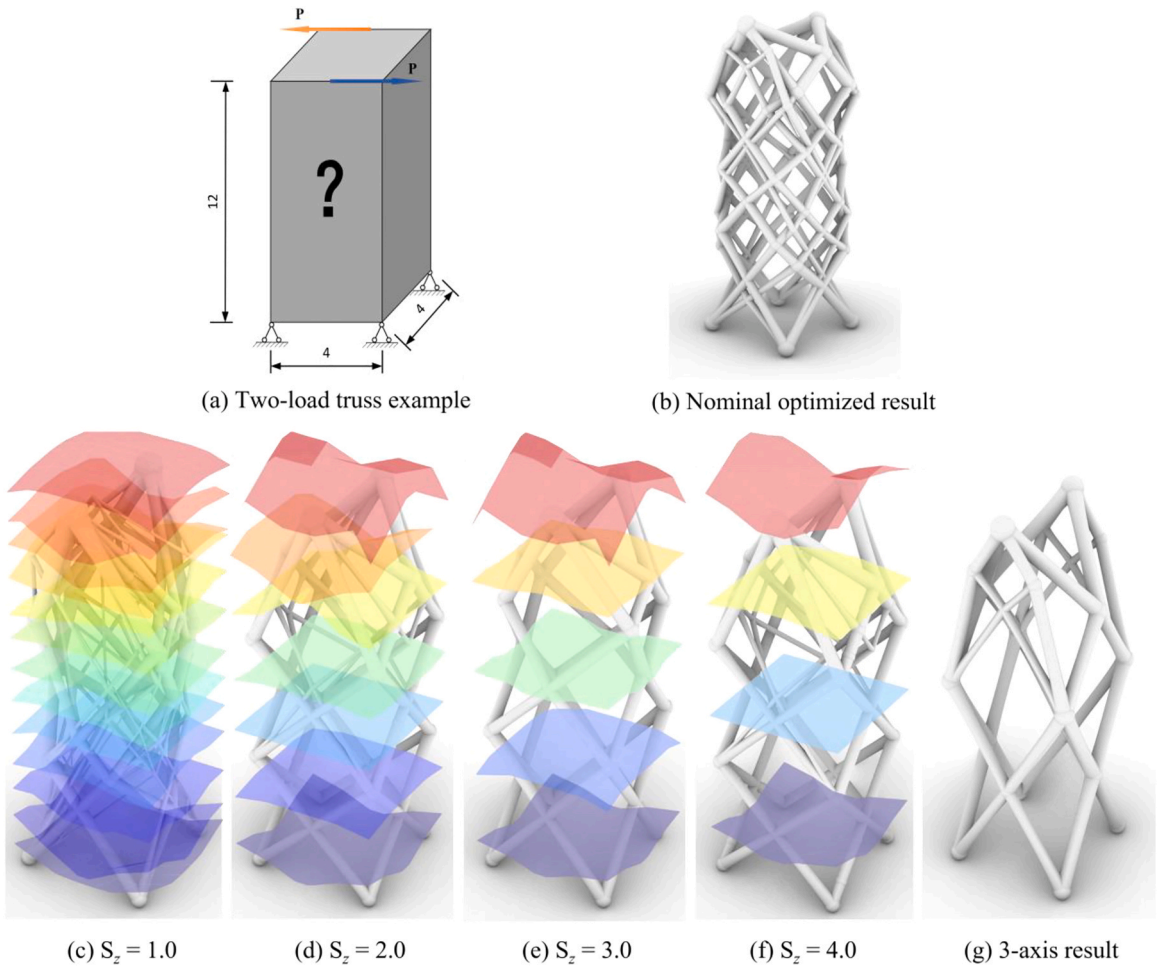

Fig. 15. Two loads truss example: (a) case description. (b) Nominal optimized result without considering overhang constraints. Compared to (b), (c) optimized structure with curved printing plan and $S_z = 1.0$, the volume increase is 5.10 %; (d) optimized structure with curved printing plan and $S_z = 2.0$, the volume increase is 1.11 %; (e) optimized structure with curved printing plan and $S_z = 3.0$, the volume increase is 0.35 %; (f) optimized structure with curved printing plan and $S_z = 4.0$, the volume increase is 1.13 %; (g) optimized structure with horizontal printing plan, the volume increase is 12.43 %.

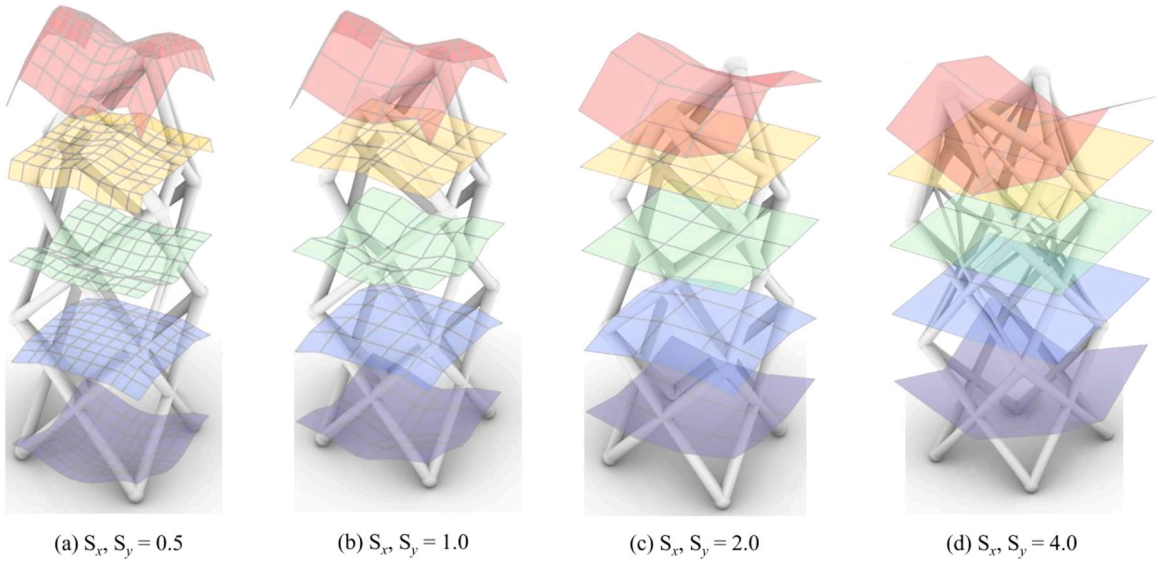

Fig. 16. Two loads truss example: Compared to result without considering overhang constraints, (a) optimized structure with curved printing plan and S_x, S_y are set to 0.5, the volume increase is 0.91 %; (b) optimized structure with curved printing plan and S_x, $S_y = 1.0$, the volume increase is 0.82 %; (c) optimized structure with curved printing plan and S_x, $S_y = 2.0$, the volume increase is 0.61 %; (d) optimized structure with curved printing plan and S_x, $S_y = 4.0$, the volume increase is 1.21 %.

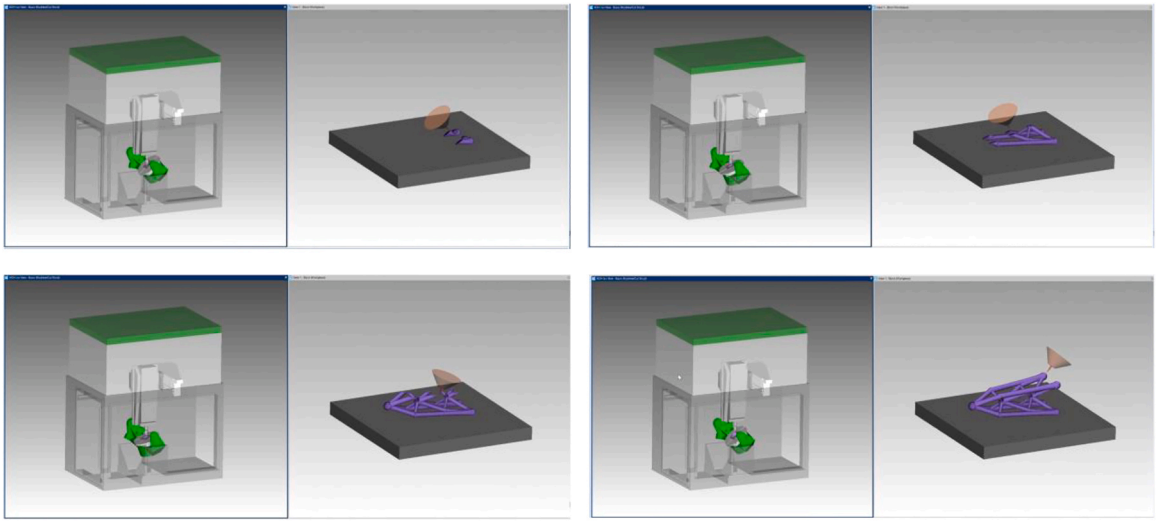

Fig. 17. Multi-axis printing simulation of the optimized cantilever shown in Fig. 14(g).

sizes S_x, S_y are shown in Fig. 16(a - d). The result shows that large horizontal sizes increase the structure complexity (Fig. 16(d)). Nevertheless, the variation of horizontal zone sizes results in a minor effect on the structural volume.

5. Multi-axis printing tests

In this section, we first validate the optimized results through a numerical printing simulation. As illustrated in Fig. 13, the printing process begins with Layer 1 at the bottom and progresses upward, completing each layer sequentially. The simulation is conducted using VERICUT with the BeAM Magic 2.0 5-axis machine. The printing paths for the optimized structures shown in Figs. 14(g) and 15(e) are generated and simulated, with several intermediate states depicted in Figs. 17 and 18. Throughout the entire printing process for both structures, no collisions were detected. Detailed videos of the simulations can be found in the Support Videos section.

Beyond the numerical validations, the optimized structure shown in Fig. 13 is physically printed using the multi-axis 3D printing machine depicted in Fig. 19, validating the feasibility of the proposed approach. A video of the printing process can be found in the Support Videos section.

In this experiment, the wire feeding and heating systems are integrated into the robot arm. The Fused Deposition Modeling (FDM) printing nozzle is mounted on a KUKA robot arm (KR 10 R1100-2), while the base platform below is mounted on an external arm, providing two additional degrees of freedom (i.e., spin and tilt). The tilting axis can rotate up to $\pm$ 120°, and the base platform has a radius of 200 mm. The distance from the base platform surface to the tilt central axis is 170 mm. A KUKA smartPAD controls the multi-axis printing machine during the printing process.

The bounding box of the printed model from Fig. 13 measures 60 mm $\times$ 60 mm $\times$ 120 mm. PLA wires of 1.75 mm diameter are used for printing; the nozzle diameter is 0.6 mm; the nozzle temperature is set to 210°C; the hotbed temperature is 50°C; the layer height is 0.4 mm, and the printing speed is 30 mm/s.

The creation of the printing tool paths involves three steps, as illustrated in Fig. 20. First, a structural model in STL format is generated in Rhino [49], based on the nodal coordinates and member cross-sectional areas from the optimized structure [50]. Next, the model is sliced using the printing surfaces obtained during the optimization process (as seen in Fig. 13(a)), which yields layers of outline tool paths. Each layer is then filled with inner tool paths using a zigzag pattern [51], with a 0.4 mm spacing and a 0.1 mm shrink length (shown in Fig. 18(c)).

Various build directions are utilized during the printing process, with

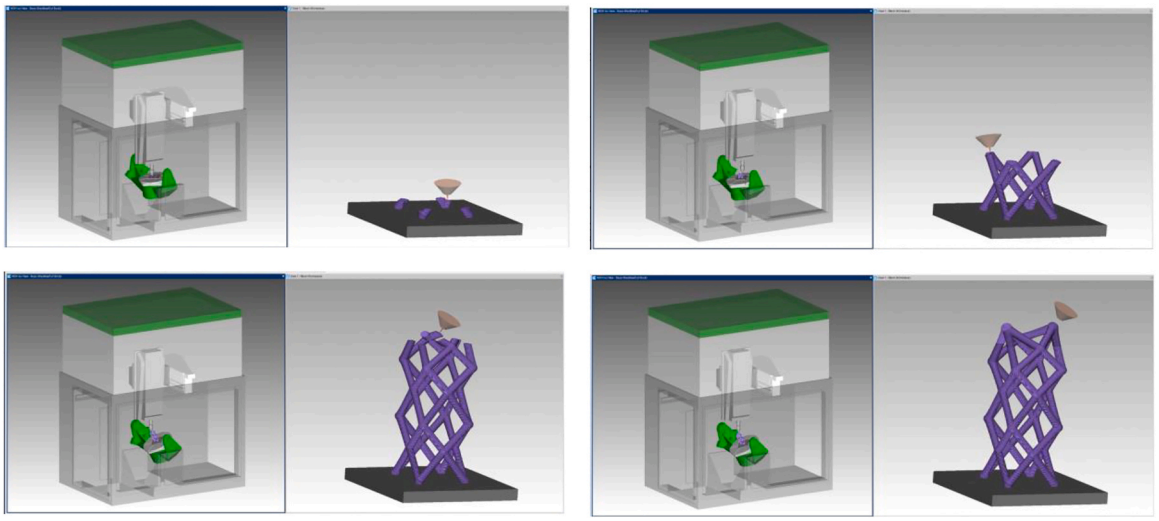

Fig. 18. Multi-axis printing simulation of the optimized cantilever shown in Fig. 15(e).

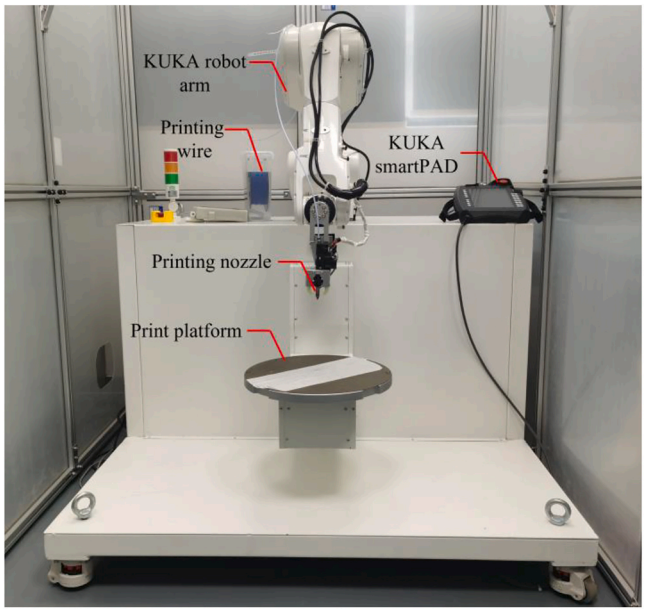

Fig. 19. Photo of multi-axis AM machine used in the printing test.

several photos for the intermediate printing states and completed model shown in Fig. 21. By employing the optimized printing surfaces from Fig. 13, the entire printing process is completed without the need for support and is collision-free.

It is worth noting that the printed structure exhibits minor surface defects, such as the member C marked in Fig. 21(e). The occurrence of these defects is due to: (1) the sudden change in local build direction causes surface gouging, which has been previously reported in [52]; (2) the multi-axis machine employed exhibits a constant machine error on the movement of the base platform, which measures at ≈ 1 mm at 90° tilting angles. The first problem can be addressed by customizing the printing tool path to allow for a smooth transition of local build directions [53]. The second issue can be addressed by measuring the movement errors at different tilting angles, and then incorporating error correction into the generation process of the printing tool paths.

Nevertheless, it is evident that the overhang effect is successfully addressed utilizing the proposed approach. The most overhanging structural members are members A and B marked in Fig. 21(e), which have an overhang angle of 19°. To accommodate the overhang effect, a build direction associated with a 59.3° tilting angle is utilized as shown in Fig. 21(a). As a result, these two members are printed without any supporting structures, highlighting the effectiveness of the proposed approach.

6. Discussion

The examples presented in Sections 4 and 5 demonstrate that the proposed approach can effectively yield efficient and buildable structures by leveraging multi-axis AM. Future studies could enhance this approach by incorporating additional factors. For instance, research indicates that mechanical performance for truss structures under axial loading is dependent on the printing direction [54,55]. Therefore, integrating mechanical performance factors into the current approach, supported by sufficient experimental data, could be a valuable direction for future research.

Additionally, in large-scale AM projects, size constraints often require decomposing the structure into multiple parts, printing each part separately, and then assembling them. Therefore, developing an optimization approach that can automatically manage the decomposition

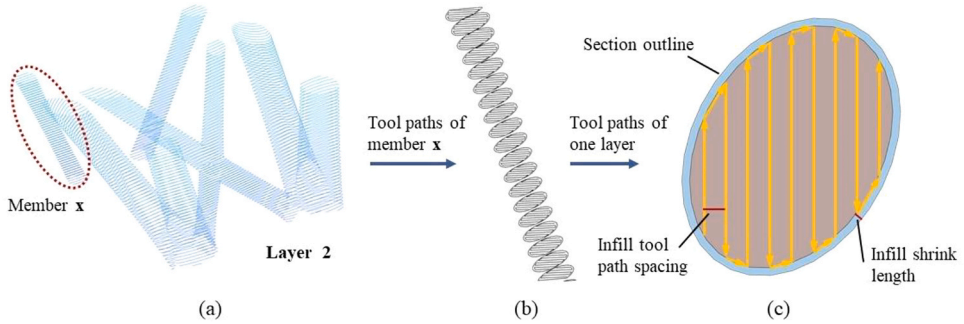

Fig. 20. Slicing process for printing models in Fig. 13.

Fig. 21. Photos of the model printing process, where (a-d) depict intermediate printing states, and (e) shows the completed model. Notably, in (e), the members with the highest overhang angle, A and B, are printed successfully without the need for supports. However, a minor defect is observed in the top member C, attributable to a mechanical motion error in the rotatable base-platform.

process while integrating multi-axis AM for producing the parts would be highly valuable for future research.

7. Conclusions

This paper introduces a method to consider truss layout optimization with overhang constraints. Specifically, the overhang constraints are considered based on multi-axis additive manufacturing, with both the structure and the associated local build directions concurrently designed in the optimization process. A two-step optimization scheme is proposed. The first step employs a novel optimization problem focused on determining the printing surfaces for a given optimized structure. However, since the structure remains unchanged in this step, the overhang problem may not be eliminated. To address this, the second step employs a comprehensive optimization to simultaneously refine the structure and the printing surfaces. This aims to further enhance structural efficiency while minimizing overhang. Given the non-linear and non-convex nature of this comprehensive problem, we also introduce an iterative approach to improve the quality of initial solutions for the second step. The effectiveness of our proposed method is illustrated through several numerical examples. Furthermore, we have physically validated one of the optimized structures using a multi-axis AM machine. Based on the results, we draw the following conclusions:

(1) To assess the effectiveness of different methods, we employ the nominal solution derived from traditional layout optimization as a benchmark, using it to measure the increase in volume attributable to the overhang constraint. The multi-axis configuration-based approach showcases superior adaptability over the 3-axis configuration-based techniques. For instance, in the cantilever example shown in Fig. 14, the volume increase observed with the three-axis-based method, standing at 117.19 %, is significantly reduced to 1.85 % by adopting the multi-axis-based approach.
(2) The selection of partition spacing directly impacts the optimization results. When the partition boundaries align closely with the nodes, results with relatively low material consumption can be achieved in the proposed iterative processes.
(3) During the physical validation, although the variation in local build directions led to minor surface defects, the overhang effect was successfully eliminated.

Therefore, the proposed approach can lead to self-supporting structures with negligible compromise on the optimized volume, demonstrating a significant advancement in the design and manufacturing of efficient truss structures for additive manufacturing.

CRediT authorship contribution statement

Jun Ye: Writing – review & editing, Supervision, Project administration, Methodology, Funding acquisition, Conceptualization. **Xiaoyang Lin:** Writing – original draft, Software, Methodology, Investigation. **Guan Quan:** Writing – review & editing, Methodology, Conceptualization. **Cheng Huang:** Writing – review & editing, Methodology. **Hongjia Lu:** Writing – review & editing, Supervision, Methodology, Investigation, Conceptualization. **Linwei He:** Writing – review & editing, Software, Methodology. **Paul Shepherd:** Writing – review & editing, Methodology.

Declaration of Competing Interest

The authors declare that they have no known competing financial interests or personal relationships that could have appeared to influence the work reported in this paper.

Acknowledgements

Finally, the authors would like to express their gratitude to the National Natural Science Foundation of China (Project No.52208215) for its financial support for the work of this project. Additionally, appreciation is extended to the INTEGRADDE project, part of the European Union's Horizon 2020 research and innovation programme (Grant No. 820776), which provided the foundational research critical to this study.

Data availability

Data will be made available on request.

References

[1] Pajonk A, Prieto A, Blum U, Knaack U. Multi-material additive manufacturing in architecture and construction: a review. J Build Eng 2022;45:103603.
[2] Tuazon BJ, Custodio NA, Basuel RB, Delos LA, Dizon JR. 3D printing technology and materials for automotive application: a mini-review. Key Eng Mater 2022;913:3–16.
[3] Omiyale B.O., Olugbade T.O., Abioye T.E., Farayibi P.K.Wire arc additive manufacturing of aluminium alloys for aerospace and automotive applications: A review, J. Mater. Sci. 38(7) (2022) 391-408..
[4] Madhavadas V, Srivastava D, Chadha U, Raj SA, Sultan MT, Shahar FS, et al. A review on metal additive manufacturing for intricately shaped aerospace components. Cirp J Manuf Sci Tec 2022;39:18–36.
[5] Salmi M. Additive manufacturing processes in medical applications. Materials 2021;14(1):191.
[6] Hadjipantelis N, Weber B, Buchanan C, Gardner L. Description of anisotropic material response of wire and arc additively manufactured thin-walled stainless steel elements. Thin-Walled Struct 2022;171:108634.
[7] Lakhdar Y, Tuck C, Binner J, Terry A, Goodridge R. Additive manufacturing of advanced ceramic materials. Prog Mater Sci 2021;116:100736.
[8] Liu B, Shen H, Zhou Z, Fu J. Research on support-free WAAM based on surface/interior separation and surface segmentation. J Mater Process Tech 2021;297:117240.
[9] Li Y, He D, Yuan S, Tang K, Zhu J. Vector field-based curved layer slicing and path planning for multi-axis printing. Robot Cim-Int Manuf 2022;77:102362.
[10] Dai C, Wang CC, Wu C, Lefebvre S, Fang G, Liu YJ. Support-free volume printing by multi-axis motion. ACM Trans Graph 2018;37(4):1–14.
[11] Xu K, Li Y, Chen L, Tang K. Curved layer based process planning for multi-axis volume printing of freeform parts. Comput -Aided Des 2019;114:51–63.
[12] Li Y, He D, Wang X, Tang K. Geodesic distance field-based curved layer volume decomposition for multi-axis support-free printing. arXiv Prepr arXiv 2020;2003:05938.
[13] Bi D, Xie F, Tang K. Generation of efficient iso-planar printing path for multi-axis FDM printing. J Manuf Mater Proc 2021;5(2):59.
[14] Michell AG. The limits of economy of material in frame-structures. Lond Edinb Philos Mag J Sci 1904;8(47):589–97.
[15] Bendsøe MP, Kikuchi N. Generating optimal topologies in structural design using a homogenization method. Comput Methods Appl Mech 1988;71(2):197–224.
[16] Sigmund O. A 99 line topology optimization code written in Matlab. Struct Multidiscip Optim 2001;21:120–7.
[17] Querin OM, Steven GP, Xie YM. Evolutionary structural optimisation (ESO) using a bidirectional algorithm. Eng Comput 1998;15(8):1031–48.
[18] Querin OM, Young V, Steven GP, Xie YM. Computational efficiency and validation of bi-directional evolutionary structural optimisation. Comput Methods Appl Mech 2000;189(2):559–73.
[19] Allaire G, Jouve F, Toader AM. A level-set method for shape optimization. Cr Math 2002;334(12):1125–30.
[20] Allaire G, Jouve F, Toader AM. Structural optimization using sensitivity analysis and a level-set method. J Comput Phys 2004;194(1):363–93.
[21] Wang MY, Wang X, Guo D. A level set method for structural topology optimization. Comput Methods Appl Mech 2003;192(1-2):227–46.
[22] Guo X, Zhang W, Zhong W. Doing topology optimization explicitly and geometrically—a new moving morphable components based framework. J. Appl. Mech-T, 81. ASME; 2014.
[23] Zhang W, Yuan J, Zhang J, Guo X. A new topology optimization approach based on Moving Morphable Components (MMC) and the ersatz material model. Struct Multidiscip Optim 2016;53:1243–60.
[24] Zhang W, Yuan J, Zhang J, Guo X. Lagrangian description based topology optimization—a revival of shape optimization. Appl Mech-T ASME 2016;83(4).
[25] Guo X, Zhang W, Zhang J, Yuan J. Explicit structural topology optimization based on moving morphable components (MMC) with curved skeletons. Comput Methods Appl Mech 2016;310:711–48.
[26] Zhang W, Yang W, Zhou J, Li D, Guo X. Structural topology optimization through explicit boundary evolution. Appl Mech-T ASME 2017;84(1).
[27] Zhang W, Chen J, Zhu X, Zhou J, Xue D, Lei X, et al. Explicit three dimensional topology optimization via Moving Morphable Void (MMV) approach. Comput Methods Appl Mech 2017;322:590–614.
[28] Dorn WS. Automatic design of optimal structures. J De Mec 1964;3:25–52.

[29] Gilbert M, Tyas A. Layout optimization of large-scale pin-jointed frames. Eng Comput 2003;20(8):1044–64.
[30] He L, Gilbert M. Rationalization of trusses generated via layout optimization. Struct Multidiscip Optim 2015;52:677–94.
[31] He L, Pritchard T, Maggs J, Gilbert M, Lu H. Peregrine Use Man 2022.
[32] Fairclough HE, He L, Pritchard TJ, Gilbert M. LayOpt: an educational web-app for truss layout optimization. Struct Multidiscip Optim 2021;64(4):2805–23.
[33] Sigmund O, Aage N, Andreassen E. On the (non-) optimality of Michell structures. Struct Multidiscip Optim 2016;54:361–73.
[34] Garaigordobil A, Ansola R, Fernandez I. de Bustos, On preventing the dripping effect of overhang constraints in topology optimization for additive manufacturing. Struct Multidiscip Optim 2021;64(6):4065–78.
[35] Gaynor AT, Guest JK. Topology optimization considering overhang constraints: Eliminating sacrificial support material in additive manufacturing through design. Struct Multidiscip Optim 2016;54(5):1157–72.
[36] Garaigordobil A, Ansola R, Santamaría J, Fernández I. de Bustos, A new overhang constraint for topology optimization of self-supporting structures in additive manufacturing. Struct Multidiscip Optim 2018;58(5):2003–17.
[37] Langelaar M. Topology optimization of 3D self-supporting structures for additive manufacturing. Addit Manuf 2016;12:60–70.
[38] Langelaar M. An additive manufacturing filter for topology optimization of print-ready designs. Struct Multidiscip Optim 2017;55(3):871–83.
[39] van de Ven E, Maas R, Ayas C, Langelaar M, van Keulen F. Continuous front propagation-based overhang control for topology optimization with additive manufacturing. Struct Multidiscip Optim 2018;57(5):2075–91.
[40] van de Ven E, Maas R, Ayas C, Langelaar M, van Keulen F. Overhang control in topology optimization: a comparison of continuous front propagation-based and discrete layer-by-layer overhang control. Struct Multidiscip Optim 2021;64(2):761–78.
[41] He L, Gilbert M, Johnson T, Pritchard T. Conceptual design of AM components using layout and geometry optimization. Comput Math Appl 2019;78(7):2308–24.
[42] Lu H, He L, Gilbert M, Gilardi F, Ye J. Design of optimal truss components for fabrication via multi-axis additive manufacturing. Comput Methods Appl Mech 2024:418–116464.
[43] Ye J, Guo Q, Lu H, Kyvelou P, Zhao Y, Gardner L, et al. Topology optimisation of self-supporting structures based on the multi-directional additive manufacturing technique. Virtual Phys Prototy 2023;18(1):e2271458.
[44] A.R. Nassar, E.W. Reutzel, Beyond Laser-by-Laser Additive Manufacturing-Voxel-Wise Directed Energy Deposition, 2014 International Solid Freeform Fabrication Symposium, University of Texas at Austin (2015).
[45] Xu K, Li Y, Chen L, Tang K. Curved layer based process planning for multi-axis volume printing of freeform parts. Comput -Aided Des 2019;114:51–63.
[46] MOSEK. ApS, Mosek optimizer API for Python, Version 9.17 (2022) 6-4. URL: ⟨https://docs.mosek.com/latest/pythonapi/index.html⟩.
[47] Wächter A, Biegler LT. On the implementation of an interior-point filter line-search algorithm for large-scale nonlinear programming. Math Program 2006;106:25–57.
[48] Haftka RT, Gürdal Z. Elements of structural optimization. SSBM 2012;11.
[49] Rhinoceros 7, URL: ⟨https://www.rhino3d.com/⟩, 2021.
[50] Smith CJ, Gilbert M, Todd I, Derguti F. Application of layout optimization to the design of additively manufactured metallic components. Struct Multidiscip Optim 2016;54(5):1297–313.
[51] Pan ZX, Ding DH, Wu BT, Cuiuri D, Li HJ, Norrish J. Arc welding processes for additive manufacturing: a review. Trans Intell Weld Manuf 2018;1(1):3–24.
[52] Li Y, He D, Yuan S, Tang K, Zhu J. Vector field-based curved layer slicing and path planning for multi-axis printing. Robot Cim-Int Manuf 2022;77:102362.
[53] Xie F, Jing X, Zhang C, Chen S, Bi D, Li Z, et al. Volume decomposition for multi-axis support-free and gouging-free printing based on ellipsoidal slicing. Comput -Aided Des 2022;143:103135.
[54] Hadjipantelis N, Weber B, Buchanan C, Gardner L. Description of anisotropic material response of wire and arc additively manufactured thin-walled stainless steel elements. Thin-Walled Struct 2022;171:108634.
[55] Gardner L. Metal additive manufacturing in structural engineering–review, advances, opportunities and outlook. Structures 2023;47:2178–93.